Well injectivity during CO2 storage operations in deep saline aquifers–Part 1: Experimental investigation of drying effects, salt precipitation and capillary forces

Yannick Peysson, Laurent André, Mohamed Azaroual

Well injectivity during CO_2 storage operations in deep saline aquifers

1: Experimental investigation of drying effects, salt precipitation and capillary forces

Yannick Peysson[a], Laurent André[b], Mohamed Azaroual[b]

[a]*IFPEN, 1 et 4 Avenue de Bois-Préau, 92 852 Rueil-Malmaison Cedex – France*

[b]*BRGM, Water, Environment and Ecotechnologies Direction, 3 Avenue Claude Guillemin, BP 36 009, F-45 060 Orléans Cedex 2 – France*

Submitted to

International Journal of Greenhouse Gas Control

Abstract

Carbon Capture and Storage (CCS) is a technique than can potentially limit the accumulation of greenhouse gases in the atmosphere. Well injectivity issues are of importance for CCS because the gas injection rate must be maintained at a high level (a million tonnes of CO_2 per year and per site) during the industrial operation period (30 to 40 years). The risk of altered permeability must therefore be determined in order to guarantee the sustainability and the security of the CO_2 geological storage. Injection of dry gas in deep saline aquifers might lead to near wellbore drying and salt precipitation. The solid salt might then reduce the rock permeability by clogging pores or by pore throat restriction. The objective of this paper is to present new experimental results on the drying of rocks induced by continuous injection of large amount of dry gas (N_2). The main goal of the study was to understand and model the physical processes that govern the decrease in water saturation in reservoir rocks.

Two types of sandstone were used to study slow and fast drying rates and capillary effects on drying. The experimental results evince the main physical parameters that control the key mechanisms. In a companion paper in this issue (André et al., 2013), we show that the continuous approach in the context of a compositional two-phase flow model can fairly well predict the saturation evolution in the near wellbore and the alteration in permeability due to salt precipitation.

Keywords: drying-out effects, coupled modelling, relative permeability, salt precipitation, capillary processes.

1. Introduction

Geological sequestration of CO_2 into deep saline aquifers is of interest because these geological formations represent a huge storage volume. However, they have been studied much less than mature oil & gas reservoirs. Injection of carbon dioxide into saline aquifers might involve some specific effects that could limit the gas injectivity. Different mechanisms could alter the permeability. One of the first studied is geochemical reactions due to CO_2 injection (Kaszuba et al., 2003; Jonhson et al., 2004; Brosse et al., 2005; lagneau et al., 2005; André et al., 2007, 2010). The dissolution of the carbon dioxide in water can induce mineral precipitation and dissolution. The rock porosity and permeability can then be modified depending mainly on the rock type but also on injection conditions (Bacci et al., 2011a). Another mechanisms, much less studied, is drying and salt precipitation at the near wellbore. The dry injected gas, at low water-vapour partial pressure, will equilibrate with the groundwater and water mass transfer will occur leading to the desiccation of the rock. Drying effect has been studied in the context of oil & gas to estimate *water blocking* in the case of gas production well (Mahadevan et al., 2006, 2007) but drying can also induce salt precipitation in the case of saline aquifer. The solid salt might reduce the rock permeability by clogging pores or by pore throat restriction. This effect has been reported for gas producing wells in reservoirs of high salinity brine (Kleinitz et al., 2003). In the context of CO_2 geological storage, injectivity alteration by salt precipitation has been analytically and numerically studied by Giorgis et al. (2007), Pruess and Müller (2009), Pruess (2009) and Zeidouni et al. (2009). They showed that skin factors due to salt precipitation effects can be evaluated. Flow models have been used to study drying and precipitation dynamics in simplified well bore geometry taking into account a larger set of parameters (Spycher et al., 2003; Spycher and Pruess, 2005; André et al., 2007). The results reveal large drying zones in certain cases. Recent experimental work has attempted to measure the change in permeability under controlled drying conditions and has shown that permeability can alter significantly (Bacci et

al., 2011b; Ott et al., 2011; Peysson et al., 2011a; Peysson, 2012; Golghanddashi et al., 2013).

The expansion with time of dried zones near injection wells has been studied for the most part numerically, and field-scale comparison is not yet possible because few large-scale pilots have been built. Experimental studies are therefore very useful for determining the key parameters involved so that we can correctly model well injectivity in the context of CO_2 storage. We studied the effect of long-term injection of dry gas in brine-saturated rock samples having different porosities and permeabilities in order to understand and quantify the main parameters needed to develop a comprehensive model of CO_2 injection in real situations. We specifically looked at different drying rates and capillary effects that might limit the drying by using rock samples with very different permeabilities. In a companion paper in this issue, we describe the use of reservoir numerical models to simulate drying and precipitation dynamics. The numerical results are in good agreement with the experiments described in this paper.

2. Experimental set up

2.1 Set up

The experiment involved placing cylindrical rock samples 6 cm long and 4.9 cm in diameter in a horizontal Hassler cell (Fig. 1). The inlet of the core holder is connected to a gas reservoir and the injection pressure controller. A back pressure of 50 bars was set at the outlet. Outlet gas fluxes were measured with a gas flow meter after the back pressure and the water outlet volume had been recorded using a burette. The pressure drop across the sample was also recorded. The system temperature is thermostatically controlled. An X-ray source and detector are placed on a translation rail that records the saturation profile along the sample. Calibration under dry and fully saturated conditions allows the water saturation measurements. Each saturation profile is obtained in 12 minutes.

2.2 Rocks and Fluids

Two types of sandstone with very different petrophysical properties were used for this study.

105 One is a Vosges Sandstone that is representative of a reservoir rock with 20-22% porosity
106 and a permeability of about 100 mD. The other is a Moliere Sandstone with a very low
107 permeability 10^{-2} mD and 14% porosity. The Moliere Sandstone, which cannot be considered
108 to be representative of a reservoir rock, was chosen to study the effect of capillary trapping
109 on drying dynamics since capillary effects are enhanced in tight systems, and to test the
110 model more broadly and specifically in the low drying rate regime. The rock properties are
111 summarized in Table 1.

112 ***Non-wetting fluid (Nitrogen)***

113 The non-wetting fluid used in this study is nitrogen (N_2) because we focused only on drying
114 mechanisms. CO_2 might have caused ancillary geochemical reactions and water-rock
115 interactions outside of the scope of this study. The key parameter needed to evaluate drying
116 dynamics is the water vapour concentration in the gas phase at thermodynamic equilibrium
117 under specific temperature and pressure conditions. The water vapour content is known for
118 different gas and water systems and specifically for water brine/CO_2 (Spycher et al., 2003;
119 Spycher and Pruess, 2005). So, the results, in term of drying dynamic, obtained using N_2 can
120 be used for CO_2 storage based on reservoir modelling with appropriate thermodynamic
121 description of the carbon dioxide/brine system.

122 ***Brine***

123 Various brines were prepared for the experiments. With the Moliere sandstone, we used
124 mainly a mixture of salt representative of a Paris Basin brine at a high salinity of 160 g/L (KCl
125 4.12 g/L; $MgCl_2,6H_2O$ 5.23 g/L; $CaCl_2,2H_2O$ 22.00 g/L; NaCl 139.33 g/L; Na_2SO_4 0.52 g/L)
126 (Azaroual et al., 1997). For the Vosges sandstone, we used a mixture of aqueous KCl and KI
127 solutions. The latter is used to intensify the density contrast for X-ray measurements.

128 ***2.3 Methodology***

129 The rock sample cores were initially dried in an oven at 80 °C for at least 24 hours and
130 placed in the core holder. A first X-ray profile under dry conditions was acquired before the
131 sample was saturated with the brine. A second X-ray profile was acquired in order to

132 calibrate the X-ray absorption technique for saturation measurements. The initial water
133 permeability was then determined by measuring the flow rate and pressure. The nitrogen
134 was then injected under controlled pressure. The inlet pressure was fixed and the outlet gas
135 flow rate was measured. Saturation profiles were recorded repeatedly to measure the
136 evolution of brine saturation in the samples.
137
138 **3. Drying of Moliere Sandstone samples by gas injection**
139 The dynamics of drying by gas injection have been only poorly investigated by experiments
140 (Mahadevan et al., 2007; Peysson et al., 2011b). The main objective of our work was to
141 measure the evolution of water saturation with time in order to quantify the drying effect. Is
142 there a remaining water phase blocked by capillary effects? What effect does the dissolved
143 salt have on drying dynamics and rock permeability? These questions must be answered if
144 we wish to predict, for CO_2 sequestration, the temporal and spatial evolution of the dry zone
145 near the injection wells. The first set of experiments was done with tight sandstone to
146 increase the capillary effects and to investigate the drying dynamics.
147 **3.1 Drying conditions at the lab scale and experimental results**
148 We measured the evolution of the local and average liquid saturation in the Moliere sample.
149 The nitrogen injection was imposed in four steps (Fig. 2). The outlet pressure was set at 50
150 bars and two temperatures were studied: 90 °C and 120 °C.
151 The pressure was increased step-wise to study the effect of gas velocity on saturation and
152 drying dynamics. The average water saturation and the outlet gas flow rates for the two
153 temperatures are shown in Fig. 3, and the local saturation profiles are shown in Fig. 4.
154 At both temperatures, the mean water saturation decreased and the gas outlet flow rate
155 increased (Fig. 3). During the first two pressure plateaus, the predominant regime was a two-
156 phase immiscible displacement (piston effect) as the gas flow pushed the water out of the
157 rock sample. Thereafter, the gas flow rate was high enough to evacuate part of the water as
158 water vapour in the gas phase (last two plateaus). In this regime, the water saturation

decreased below the irreducible water saturation level (S_{wi} = 16%). At the same time, the gas flow rate increased significantly. At 90°C, water saturation reached zero, and at 120°C, it reached a “residual signal”. In both experiments, the samples were, in fact, completely dry. To check that, we removed the samples and let them dry in an oven with regular weighting. In both cases, no mass losses were observed. The “residual signal” at 120 °C corresponds to the presence of precipitated salt in the sample measured with the X-ray.

The temporal evolution of the water saturation profiles also shows two trends (Fig. 4). The first two pressure steps are characteristic of two-phase immiscible displacement with a gas breakthrough and a decrease of the water saturation with a capillary fringe. (Because of diffraction effects, the two ends of the sample are fuzzy and we do not have the water saturation measurements at the ends. However, we clearly see the increase in saturation at the end of the sample.) However, for the last two pressures steps and at both temperatures, the profiles tend to flatten out and the capillary fringe disappears. Moreover, no drying front is observed until the end of the experiments, which means that capillary flows were strong enough to homogenise the water profiles even at low saturation.

At the end of the experiments, we observe no residual signal at 90 °C aside from a small effect at the entrance (x < 5mm), and a flat profile with a peak at the entrance at 120 °C. In both cases, precipitated salt is present in the sample.

Permeability, measured at the end of the experiments, had decreased due to the presence of salt. The final gas permeability was 37 and 50 % of the initial permeability at 90 °C and 120 °C, respectively. Every sample was weighed at the end of the experiment, but the small mass changes just allow estimating a porosity change of about one point or less.

3.2 Quantitative Interpretation - Two phase flow immiscible displacement

The results are representative of gas injection for CO_2 storage in the sense that two coupled mechanisms contribute to the changes in wellbore water saturation: viscous displacement and drying. In order to fully interpret the experiments quantitatively, we studied the effect of two-phase flow on the total water saturation evolution. Darcy's law model for two-phase flow

186 (Kulkarni et al., 2009) was used to calculate the evolution in saturation caused by the
187 injection of gas at an imposed pressure. Two closure laws are required: the gas-water
188 capillary pressure and the gas-water relative permeability curves (Fig. 5).

189 The drainage capillary pressure curve was measured using the centrifuge technique and
190 modelled with the following equation (Fig. 5a):

191 $$P_c(S_w) = -P_0 \ln(S^*) + P_t \quad (1)$$

192 where P_t and P_0 are parameters and $S^* = (S_w-S_{min})/(S_{max}-S_{min})$ is the reduced water saturation
193 (S_{min} = 0.16 and S_{max} = 1). Relative permeability curves for gas and water were calculated
194 using the Corey equation (Fig. 5b).

195 $$K_r^w = K_{\max}^w (S^*)^{\alpha_w} \quad (2)$$

196 $$K_r^g = K_{\max}^g (1 - S^*)^{\alpha_g} \quad (3)$$

197 Although the effect of temperature on relative permeability has rarely been studied, some
198 measurements are available for thermal enhanced oil recovery (Hamouda and Karoussi,
199 2008). The relative permeability curves change little for a small range of temperatures. This
200 can be interpreted, bearing in mind that these curves represent, for the most part, the
201 geometrical restriction to the flow of one phase relative to the other. The distribution of the
202 fluid in the porous structure depends on the capillarity and wettability. However, within a
203 temperature range of 90 to 120 °C, the changes are small. We therefore considered no
204 changes in the relative permeability curves for our experiments at 120 °C.

205 The capillary pressure curve can be represented as $P_c = 2.\sigma.\cos\theta/\langle r\rangle$, where <r> is the
206 average pore radius saturated with water for a given saturation. The temperature variation
207 would then be given by the surface tension variation σ and the wettability that could be
208 locally represented by a contact angle θ (or more precisely the cosines of this angle). In
209 general, surface tension decreases with temperature (Guyon et al., 2001). For water-air
210 systems, the decrease is relatively small between 90 and 120°C (60 to 55 mN/m). For the

wettability, we assume, in our case, strong water wet rock and no change with the temperature. The gas is the non-wetting phase for the two temperatures. So at a first approximation, we kept the capillary pressure curve constant for the case of 120 °C.

For the CO_2/brine system, surface tension and wettability measurements as a function of the temperature have been reported recently (Chalbaud et al., 2009, 2010).

The Darcy two phase flow equations were solved numerically. The calculated gas flow rate and the average water saturation inside the core were compared to the experimental data (Fig. 3). This confirmed that the first two pressure plateaus are essentially two-phase flow immiscible displacement. However, the two last plateaus in the experiments are dominated by drying dynamics. Indeed, with only two-phase flow, saturation should have continued to the irreducible water saturation (S_{wi} = 0.16 for these samples) but we observed a total desaturation of the samples. We must therefore quantitatively consider the effect of water evaporation.

3.3 Quantitative interpretation: Thermodynamic aspect of drying

To interpret the drying dynamics, we assumed that irreducible saturation was achieved after the gas displacement. The liquid water mobility was therefore zero. The dry gas was injected at a mass flow rate Q_g (Fig. 6). If we introduce the water vapour weight concentration at equilibrium C (kg of water/ kg of gas), the mass balance gives the outlet water flow rate CQ_g:

The decrease in the saturation in the sample is then directly related to the gas flow rate:

$$\frac{dS_w}{dt} = -\frac{C}{m_0} Q_{gaz} \tag{4}$$

where m_0 is the initial mass of water in the fully saturated sample.

In porous media, a classical assumption is to consider a local thermodynamic equilibrium so that the water vapour concentration can be calculated at equilibrium (Puiggali and Quintard, 1992). Indeed, the latent heat of the vaporisation is in excess in the solid phase and the

pores are small enough so that gas diffusion is fast enough to homogenise the water vapour at the pore scale.

Water vapour concentration

Water vapour concentration can be defined by the molar fraction y (mol of water vapour/mol of gas) or by the mass concentration C (kg of water/kg of gas). The relationship between the two variables is the following:

$$C = y\frac{M_{H_2O}}{M_{gaz}} \tag{5}$$

where M_{H2O} is the molar mass of water and M_{gas} is the molar mass (kg/mol) of the water vapour and gas mixture. For nitrogen:

$$C = y\frac{M_{H_2O}}{(1-y)M_{N_2} + yM_{H_2O}} = y\frac{M_{H_2O}}{M_{N_2}\left[1 - y\left(1 - \frac{M_{H_2O}}{M_{N_2}}\right)\right]} \tag{6}$$

But in the case of drying under our thermodynamic conditions, *y* is very small (around 10^{-3}) and the term

$$\left(1 - \frac{M_{H_2O}}{M_{N_2}}\right) = 0.36 \tag{7}$$

We could therefore simplify *C* to:

$$C = y\frac{M_{H_2O}}{M_{N_2}} \tag{8}$$

The water vapour molar fraction was estimated analytically using the Ideal Gas Law. Indeed, at equilibrium, we have:

$$y = \frac{P_s\left(\overline{T}\right)}{\overline{P}} \tag{9}$$

where $\overline{T}$ and $\overline{P}$ are the average pressure and temperature in the sample. Since we measured the volumetric flow rate in our experiments, we introduced β (kg/m^3), the water vapour concentration (mass of water vapour by volume of gas), and can write:

$$CQ_g = \beta Q^v_{gas} \tag{10}$$

where β depends only on the temperature:

$$\beta = \rho_0 \frac{P_S(\overline{T})}{P_0} \frac{M_{H_2O}}{M_{gaz}} \frac{T_0}{T} \tag{11}$$

For nitrogen, we calculated β as a function of temperature (Fig. 7) (ρ_0 = 1.17 kg/m^3 at T_0 = 20 °C and P_0 = 1.013 10^5 Pa). The vapour pressure equilibrium equation is the Duperray correlation, which represents fairly well the water vapour curve up to the critical point (P_C= 221.2 bar T_C=374.15 °C):

$$P_S(\overline{T}) = \left(\frac{\overline{T}}{100} \right)^4 \tag{12}$$

where T is °C.

We also calculated β for the real gas equation for nitrogen with CARNOT, thermodynamic software developed by IFPEN, from the Peng-Robinson equation of state. In this case, we have a weak pressure effect (Fig. 7).

Kelvin effect - Capillary contribution to the vapour concentration

Using low permeability sandstone enabled us to study capillary effects. First, we evaluated the contribution of the Laplace pressure on the liquid-vapour equilibrium. This can be evaluated from the Kelvin equation (Eq. (13)):

$$P_S^c(T) = P_S(T)\varphi \tag{13}$$

and $$\varphi = e^{-\frac{M_{H_2O} P_c(S)}{\rho RT}} \tag{14}$$

The water liquid-vapour equilibrium curve $P_s(T)$ is modified in porous media by the capillary pressure $P_c(S)$. The water is trapped in liquid form and the vapour concentration in the gas decreases. The higher the capillary pressure, the lower the water vapour concentration. But even in the Moliere sandstone, this effect was very weak, as shown by the dashed line in Fig. 7 (the correction is made for ideal gases only). We used the capillary pressure curve measured for the Moliere sandstone (Fig. 5 5a).

Saturation evolution in drying regime

From Eq. (4), if drying is the predominant regime of water evacuation, we can calculate the average saturation evolution in our experiments:

$$S_w(t) = S_w^i - \frac{\beta}{m_0}\int_0^t Q_g(t)dt \qquad (15)$$

where Q_g is the flow rate measured at the outlet of the core. Fig. 8 compares the average water saturation remaining in the sample and the saturation calculated with Eq. (15) (at 120 °C, we removed the residual signal due to the precipitated salt to have only the water saturation evolution). In Fig. 8a, we used different values of β (β_1=0.31 ; β_2=0.4 ; β_3=0.2) to compare with the data.

For the two temperatures studied, only one value of β enables a perfect estimation of the decrease in saturation. β could be measured by adjusting the saturation calculated with Eq. (15) and the experimental data.

This strong coupling between the measured gas flow rate and the average saturation was verified for all of the experiments and for the two rock types. For each experiment, in the predominant drying regime, Eq. (15) was used to calculate β and Fig. 9 shows the values measured for the different temperatures studied.

These results are very interesting because we see a very good match with β calculated with the Real Gas Law, and we can then conclude that the evaluation of β at equilibrium is valid

and that the Kelvin effect can be totally disregarded, as expected based on the model (Eq. (10)).

Outlet gas flow rate prediction in the drying mode

Because the average water saturation and the outlet gas flow rate are coupled in the drying mode (Eq. (15)), if we can determine the outlet gas flow rate from the imposed pressure, we can directly deduce the water saturation. For this, we need to know the shape of the gas relative permeability curve in the unusual range [0 - S_{wi}].

For the two experiments at different temperatures, we could directly estimate the gas relative permeability curve from the experimental data. Indeed, as shown on the local saturation profile, in the drying stage, the saturation within the sample does not depend on the position x (Fig. 4). The average water saturation depends only on time $S_w(x,t) = S_w(t)$. Under these conditions, assuming no water mobility, we can write the Darcy law directly under weak compressibility hypotheses:

$$\frac{\Delta P}{L} = \frac{\mu_g}{K_0 K_r^g\left(S_w(t)\right)} \frac{Q_g(t)}{A} \tag{16}$$

Because the pressure is constant during the plateau, we can calculate the evolution of the gas relative permeability with saturation by the ratio of Eq. (16) at two times:

$$K_r^g\left(S_w\right) = K_r^g\left(S_w(t=0)\right) \frac{Q_g(t)}{Q_g(t=0)} \tag{17}$$

The recorded data at 90 °C and 120 °C are represented in Fig. 10.

The only constraint imposed is $K^r_g(S_w=0) = 1$ (We have to recover the sample permeability in monophasic flow). The two data sets merge on a single curve (Fig. 11) that is coherent with the first set of relative permeability values estimated from the first experimental phase (two-phase flow displacement) showing that relative permeability is an effective parameter of the problem.

The results of the Fig. 11 also confirm that, as expected, relative permeability curves do not depend greatly on temperature in the 90 – 120 °C range.

3.4 Contribution of the two predominant mechanisms to the water saturation decrease

Fig. 12 shows the evolution of the average water saturation if only two-phase flow (black thin line) or only drying (bold black line) are taken into consideration. The saturation was calculated with Darcy two-phase flow model, as discussed in paragraph 3.2 (black thin line), and, using the experimental outlet gas flow rate, we calculated the equivalent water saturation evacuated through evaporation (with Eq. (11)). At the end, the mass balance of water is respected to within 3 % (water displaced through two-phase flow with water evaporated).

4. Drying experiments with Reservoir rock samples (Vosges sandstone)

4.1 Experimental results

The second set of experiments was done with Vosges sandstone – a type of rock representative of a sandstone aquifer. The initial gas permeability of the sample was 74 mD and the porosity 21.8 %. The brine was 35 g/L, a mixture of KCl (55 %wt) and KI (45 %wt). In these experiments, the imposed pressure was reduced in order to stay within the range of measurement of the gas flow rate of our system. We imposed three pressure plateaus (120 mbars, 800 mbars and 1500 mbars) and measured the gas flow rate and the saturation evolution in the sample with time. The temperature was lowered a little to decrease the evaporation rate (80 °C). The outlet pressure was 50 bars. As with the experiment at 120 °C with the Moliere sandstone, a residual absorption was obtained by the end of the drying. This time, we used this as the calibration signal for the dry state. We could then represent the evolution of the average (Fig. 13) and local liquid saturation in the sample with time (Fig. 14).

The average water saturation (Fig. 13) follows the same trend as for the Moliere samples. The first plateau is purely two-phase flow displacement with a rapid gas breakthrough (at t=5 hours) and a low gas flow rate. The second plateau is mixed, with a significant contribution of drying. For the highest pressure, drying is very rapid, lasting only a few hours.

354 The saturation profiles along the sample also show the same trend as for the Moliere
355 sandstone (Fig. 14). The first profiles are typical of two phase flow displacement with a
356 capillary fringe close to the outlet of the sample. The profiles are then flatter and at the end of
357 the drying, we clearly see a drying front that moves from the sample inlet to the outlet. This is
358 due to the fact that the drying rate is much higher than in the previous cases and the water
359 flow does not have time to re-equilibrate the water saturation in the sample.

360 The drying front is observed only at the very end of the drying stage. At higher water
361 saturation, capillary back flows are strong enough to flatten the water saturation profiles. The
362 dissolved salt is transported in the water and accumulates near the injection surface. At the
363 end of the experiment, the X-ray absorption signal is very heterogeneous throughout the rock
364 sample (Fig. 15).

365 There is a very pronounced peak in the first 5 millimetres of the sample. The residual signal
366 is due to the salt precipitation induced by the drying. The permeability decreases 70 % due to
367 this salt deposition (22 mD at the end compared to an initial 74 mD).

368 This case was numerically modelled in detail, with the full coupling of drying and two-phase
369 flow displacement (André et al., 2013).

370 We also injected gas at a constant imposed pressure of 300 mbars into a sandstone core
371 initially fully saturated with a 150 g/L of KCl brine (Fig. 16). This caused total plugging of the
372 sample. No gas flow was observed after 46 h, which confirms the previous interpretation of a
373 salt accumulation near the injection surface that can be strong enough to block the gas flow.
374 This has also been confirmed by modelling (André et al., 2013).

375 4.2 **Interpretation - Discussion**

376 The drying of the brine-saturated cores was forced by a driven gas flow. The main
377 mechanisms can be divided into two steps, as already mentioned in the literature
378 (Mahadevan et al., 2007):

- ***Step 1***: Dry gas pushes the pore water by a piston effect. The flows of the two phases (gas and brine) are controlled by Darcy equations. This is observed regardless of the initial permeability of the porous medium (Figs. 3 and 12). First, most of the water is pushed out from the core (to the outlet), then water can flow in the other direction (toward the column inlet) due to capillary effects. This process re-equilibrates the water saturation inside the core and explains the flattening of the curves observed mid-way through the experiments (Figs. 4 and 14). During this first phase, water turns also to vapour in the gas because thermodynamic equilibrium is reached as already emphasized. However, this process contributes little to the water transport compared to advection. As a consequence, in this first step, there is only little evaporation, therefore no oversaturation and salt does not precipitate.

- ***Step 2***: The water saturation in the core is close to the irreducible water saturation. Darcy brine flows are not predominant and evaporation becomes the main process within the core causing the water to be evacuated. During this phase, most of the water mass exchange takes place at the injection surface where the gas comes into contact with the water. The decrease in water saturation at the injection surface induces brine capillary back flow that transfers the brine toward the injection surface. Salt accumulates near the injection surface and precipitates when saturation is reached. This is observed in each experiment, although to a lesser extent with the Moliere sandstone (see the residual X-ray profiles for both samples at the end of the drying in Fig. 4 where there is also a small peak in the first 5 millimetres). Salt precipitation is not homogeneous because drying can cause the dissolved ions to flow toward evaporating surfaces (Huinink et al., 2002; Sgair et al., 2007; Guglielmi et al., 2008; Peysson, 2012). The salinity of the brine plays a crucial role in the amount of salt precipitated even if this mechanism is observed for all the salinities tested. In the experiment with Vosges sandstone, the brine salinity is 5 times higher than in the

405 experiment with Moliere sandstone. The consequence is a massive precipitation of
406 salt close to the inlet of the core with a full clogging preventing any gas injection.

407 The processes occurring during this second step are complex because many have opposite
408 effects. To better understand the different processes, a Péclet number can be calculated to
409 provide information concerning the ratio between advective and diffusive transport (Huinink
410 et al., 2002; Sgair et al., 2007; Guglielmi et al., 2008):

411 $$Pe = L\beta V/\rho\phi D \quad (18)$$

412 where L is the characteristic length, D the diffusion coefficient (D = 10^{-10} m^2/s for salt in
413 water), and V the gas velocity ($V = Q_g/S$). β is taken from Fig. 9.

414 During step 2 (i.e., the drying period) of the experiments with Moliere sandstone, the low
415 mean gas velocity (about 2-3 L/h) caused a very low evaporation rate. Capillary flow
416 continuously re-equilibrated the water saturation inside the core (water flowed toward the
417 sample inlet). At the same time, because of water evaporation near the injection surface, the
418 salt concentration increased, creating a salt gradient inside the column. However, the low
419 Péclet number (about 4 and 15 at 90 °C and 120 °C, respectively) suggests that salt diffusion
420 occured inside the core (from the inlet toward the outlet) resulting in a rather homogeneous
421 distribution of salt throughout the column.

422 For the experiment with the Vosges sandstone, the mean gas velocity (Q_g) was about 3
423 L/min (Fig. 13). Consequently, the Péclet number is about 360, which suggests the
424 predominance of advective processes. Massive capillary flow carried salt toward the injection
425 surface where the water evaporation was very rapid because of the gas injection flow rate.
426 Like for the previous experiments, a salt gradient was created inside the core. However,
427 because the diffusive fluxes were negligible compared to the evaporation rate, salt
428 precipitated close to the injection surface, leading to heterogeneous salt deposits.

429

430

Conclusion

We ran experiments to study the mechanisms governing the saturation evolution at the near wellbore of CO_2 injection wells. During the first stage of gas injection, two-phase flow immiscible displacement is the main mechanism and water is pushed in the aquifer. This phase could be modelled with Darcy two-phase flow models. Thereafter, the residual water at the near wellbore might be transferred to the gas phase by thermodynamic exchanges. Drying is then the predominant mechanism controlling the decrease in water saturation. The drying rate is proportional to the gas velocity and the water vapour concentration in the gas had to be estimated at equilibrium.

Any dissolved salt in the water can be transported by capillary flows induced by drying and can even accumulate near the injection surface. The permeability can then be altered by pore clogging. To correctly determine well injectivity, all of these mechanisms must be included in models to calculate the near wellbore permeability and porosity changes with time.

Acknowledgement

This work was carried out within the framework of the “Proche Puits” project, co-funded by the French National Agency for Research (ANR). The authors thank Brigitte Bazin and Elisabeth Rosenberg for fruitful discussions and Frederic Martin and Marie Claude Lynch for their help in conducting the experiments. They are also grateful to all project partners (TOTAL, GDF Suez, Schlumberger, Itasca, CNRS, University de Lorraine, University of Pau) for allowing the publication of this work.

References

André, L., Audigane, P., Azaroual, M., Menjoz A., 2007. Numerical modeling of fluid–rock chemical interactions at the supercritical CO_2–liquid interface during CO_2 injection into a carbonate reservoir, the Dogger aquifer (Paris Basin, France), Energy Conversion and Management 48, 1782–1797.

André, L., Peysson, Y., Azaroual, M., 2013. Well injectivity during CO_2 injection in deep saline aquifers - Part 2: Numerical simulations of drying, salt deposit mechanisms and role of capillary forces. International Journal of Greenhouse Gas Control, same issue.

Azaroual, M., Fouillac, C., Matray, J.M., 1997. Solubility of silica polymorphs in electrolyte solutions, II. Activity of aqueous silica and solid silica polymorphs in deep solutions from the sedimentary Paris Basin. Chemical Geology 140, 167-179.

Bacci, G., Korre, A., Durucan, S., 2011a. An experimental and numerical investigation into the impact of dissolution/precipitation mechanisms on CO_2 injectivity in the wellbore and far field regions, International Journal of Greenhouse Gas Control 5, 579-588.

Bacci, G., Korre, A., Durucan, S., 2011b. Experimental investigation into salt precipitation during CO_2 injection in saline aquifer, Energy Procedia 4, 2011, 4450-4456

Brosse, É., Magnier, C., Vincent, B., 2005. Modelling Fluid-Rock Interaction Induced by the Percolation of CO_2-Enriched Solutions in Core Samples: the Role of Reactive Surface Area, Oil & Gas Science and Technology - Rev. IFP 60(2), 287-305.

Chalbaud, C., Robin, M., Lombard, J.M., Martin, F., Egermann, P., Bertin, H., 2009. Interfacial tension measurements and wettability evaluation for geological CO_2 storage. Advance in Water Resources 32, 98–109.

Chalbaud, C., Robin, M., Lombard, J.M., Bertin, M., Egermann, P., 2010. Brine/CO_2 Interfacial Properties and Effects on CO_2 Storage in Deep Saline Aquifers. Oil & Gas Science and Technology – Rev. IFP 65 (4), 541-555.

Giorgis, T., Carpita, M., Battistelli, A., 2007. 2D modeling of salt precipitation during the injection of dry CO_2 in a depleted gas reservoir. Energy Conversion and Management 48, 1816-1826.

Golghanddashti, H., Saadat, M., Abbasi, S., Shahrabadi, A., 2013. Experimental investigation of water vaporization and its induced formation damage associated with underground gas storage, Journal of Porous Media, 16(2), 89-96.

Guglielmini, L., Gontcharov, A., Aldykiewicz, J., Stones, H.A., 2008. Drying of salt solutions in porous materials: Intermediate-time dynamics and efflorescence. Physics of Fluids, 20, 077101.

Guyon, E., Hulin, J.P., Petit, L., 2001. Hydrodynamique Physique, EDP Sciences CNRS Editions.

488 Hamouda, A., Karoussi, O., 2008. Effect of temperature, wettability and relative permeability
489 on oil recovery from oil-wet chalk. Energies 1 (1), 19–34.
490 Huinink H.P.H., Pel, L., Michels, M.A.J., 2002. How ions distribute in a drying porous
491 medium: A simple model. Physics of Fluids 14 (4), 1389-1395.
492 Johnson, J.W., Nitao, J.J., Knauss, K.G., 2004. Reactive transport modelling of CO_2 storage
493 in saline aquifers to elucidate fundamental processes, trapping mechanisms, and
494 sequestration partitioning. Lawrence Livermore National Laboratory, UCRL-JRNL-
495 205627.
496 Kaszuba, J.P., Janecky, D.R., Snow, M.G., 2003. Carbon dioxide reaction processes in a
497 model brine aquifer at 200°C and 200 bars: implications for geologic sequestration of
498 carbon. Applied Geochemistry 18, 1065–1080.
499 Kleinitz, W., Dietzsch, G., Köhler, M., 2003. Halite scale formation in gas producing wells.
500 Chemical Engineering Research and Design 81 (Part A).
501 Kulkarni, R., Watson, A.T., Nordtvedt, J.E., Sylte, A., 1998. Two-Phase Flow in Porous
502 Media: Property Identification and Model Validation. AIChe Journal 44 (11), 2337-2350.
503 Lagneau, V., Pipart A., Catalette H., 2005. Reactive transport modelling of CO_2 sequestration
504 in deep saline aquifers. Oil & Gas Science and Technology – Rev. IFP 60(2), 231–247.
505 Mahadevan, J., Sharma, M.M., Yortsos, Y.C., 2006. Flow-Through drying of porous media,
506 AIChE Journal 52, 2367–2380.
507 Mahadevan, J., Sharma, M.M., Yortsos, Y.C., 2007. Water removal from porous media by
508 gas injection: experiments and simulation. Transport in Porous Media 66, 287-309.
509 Ott, H., de Kloe, K., Marcelis, F., Makurat, A., 2011. Injection of Supercritical CO_2 in brine
510 saturated sandstone: pattern formation during salt precipitation, Energy Procedia 4,
511 4425-4432.
512 Peysson, Y., Bazin, B., Magnier, C., Kohler, E., Youssef, S., 2011a. Permeability alteration
513 due to salt precipitation driven by drying in the context of CO_2 injection. Energy
514 Procedia 4, 4387-4394.
515 Peysson, Y., Fleury, M., Blázquez-Pascual, V., 2011b. Drying Rate Measurements in
516 Convection- and Diffusion-Driven Conditions on a Shaly Sandstone Using Nuclear
517 Magnetic Resonance. Transport in Porous Media 90 (3), 1001-1016.

Peysson, Y., 2012. Permeability alteration induced by drying of brines in porous media. The European Physical Journal - Applied Physics 60, 24206p1-p12.

Pruess, K., Müller, N., 2009. Formation dry-out from CO_2 injection into saline aquifers: 1. Effects of solids precipitation and their mitigation, Water Resources Research 45, W03402.

Pruess, K., 2009. Formation dry-out from CO_2 injection into saline aquifers: 2. Analytical model for salt precipitation, Water Resources Research 45, W03403.

Puiggali, J.R., Quintard, M., 1992. Properties and simplifying assumptions for classical drying models. Advances in Drying, Publisher: Hemisphere Publishing Corporation, Chapter 4, 109-143.

Sghair, N., Prat, M., Ben Nasrallah, S., 2007. On ions transport during drying in a porous medium. Transport in Porous Media 67, 243-274.

Spycher, N., Pruess, K., Ennis-King, J., 2003. CO_2-H_2O mixtures in the geological sequestration of CO_2 I. Assessment and calculation of mutual solubilities form 12 to 100°C and up to 600 bar. Geochimica et Cosmochimica Acta 67 (16), 3015-3031.

Spycher, N., Pruess, K., 2005. CO_2-H_2O mixtures in the geological sequestration of CO_2 II. Partitioning in chloride brines at 12 to 100°C and up to 600 bar. Geochimica et Cosmochimica Acta 69 (13), 3309–3320.

Zeidouni, M., Pooladi-Darvish, M., Keith, D., 2009. Analytical solution to evaluate salt precipitation during CO_2 injection in saline aquifers. International Journal of Greenhouse Gas Control 3, 600-611.

List of Illustrations

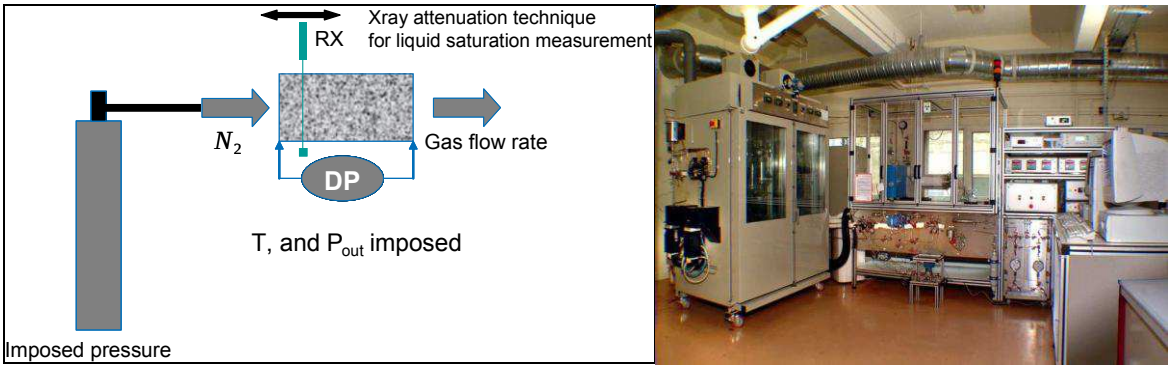

571

572 Fig. 1

573

574

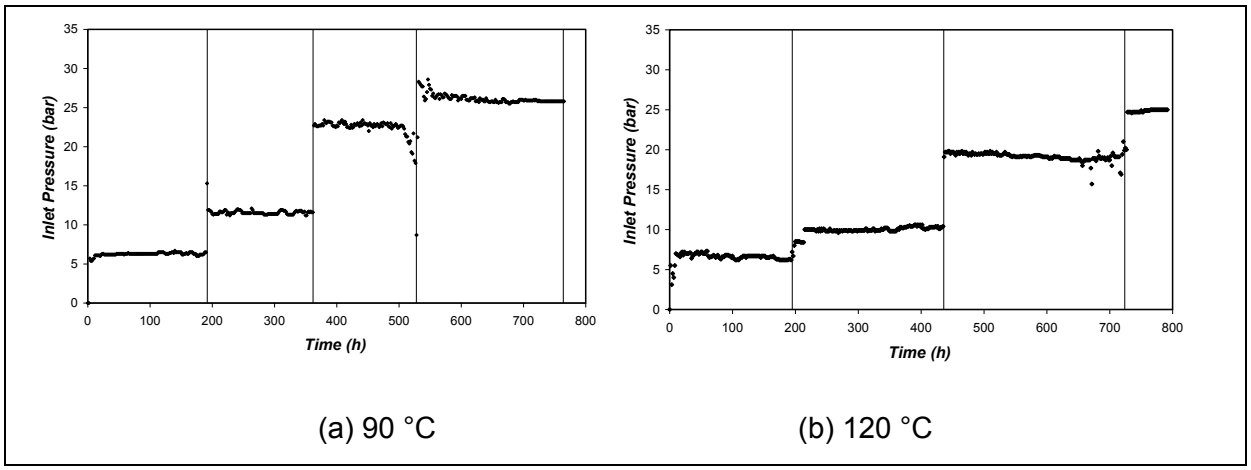

575 (a) 90 °C (b) 120 °C

576 Fig. 2

577

578

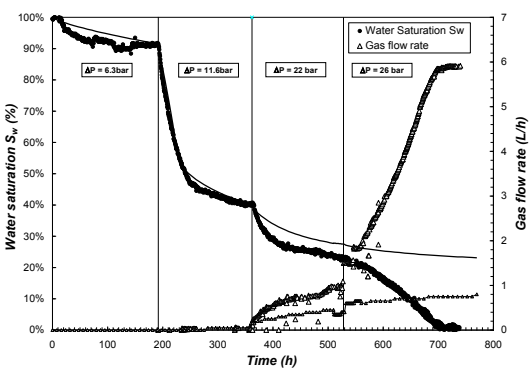

579 (a) 90°C

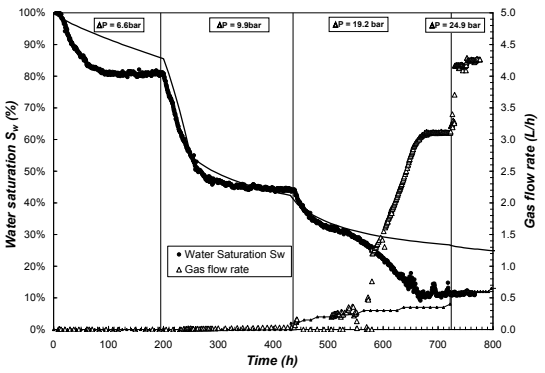

(b) 120°C

580 Fig. 3

581

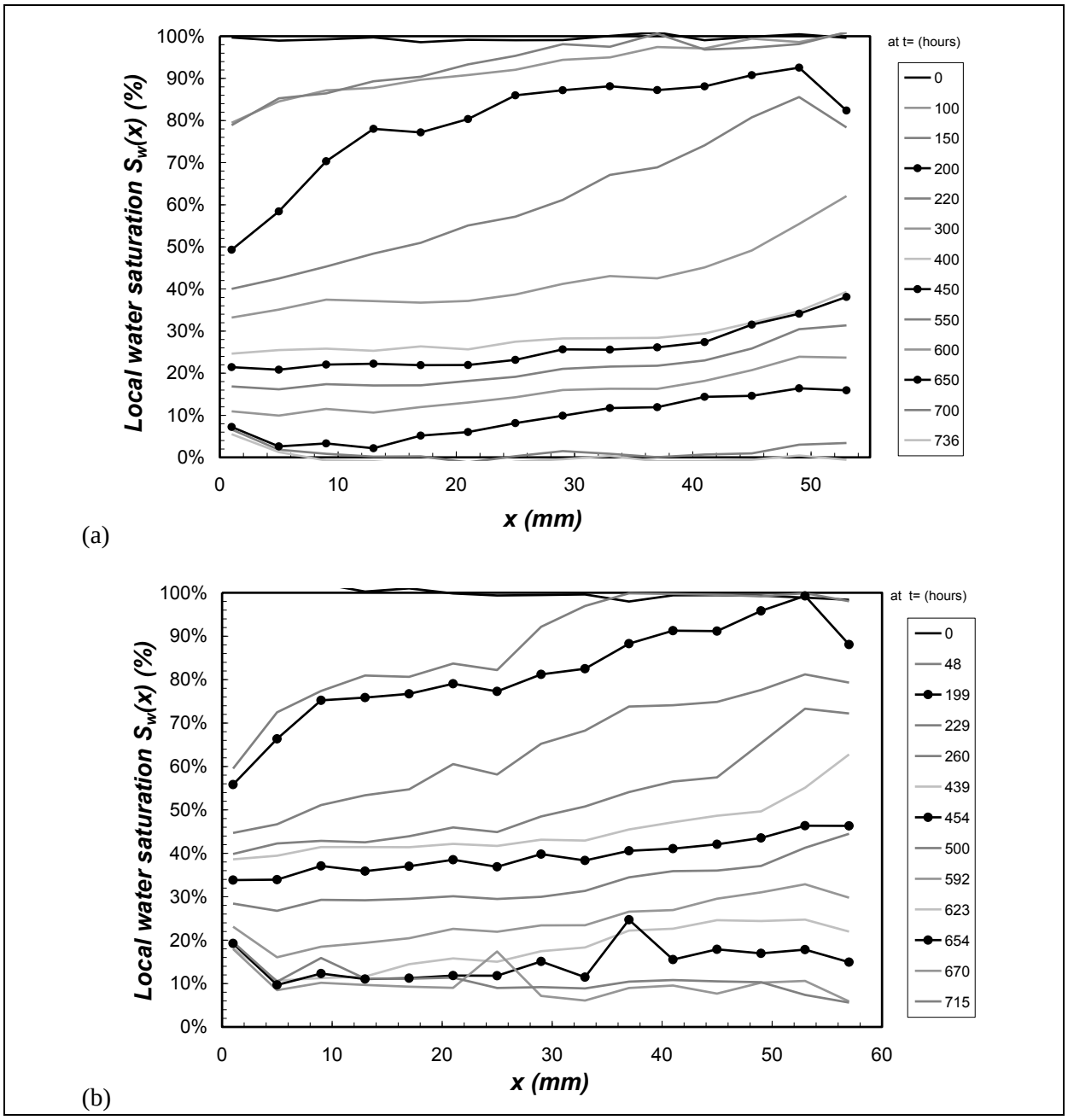
Local water saturation $S_w(x)$ (%)
100%
90%
80%
70%
60%
50%
40%
30%
20%
10%
0%
0
10
20
30
40
50
x (mm)
at t= (hours)
0
100
150
200
220
300
400
450
550
600
650
700
736
(a)
Local water saturation $S_w(x)$ (%)
100%
90%
80%
70%
60%
50%
40%
30%
20%
10%
0%
0
10
20
30
40
50
60
x (mm)
at t= (hours)
0
48
199
229
260
439
454
500
592
623
654
670
715
(b)

Fig. 4

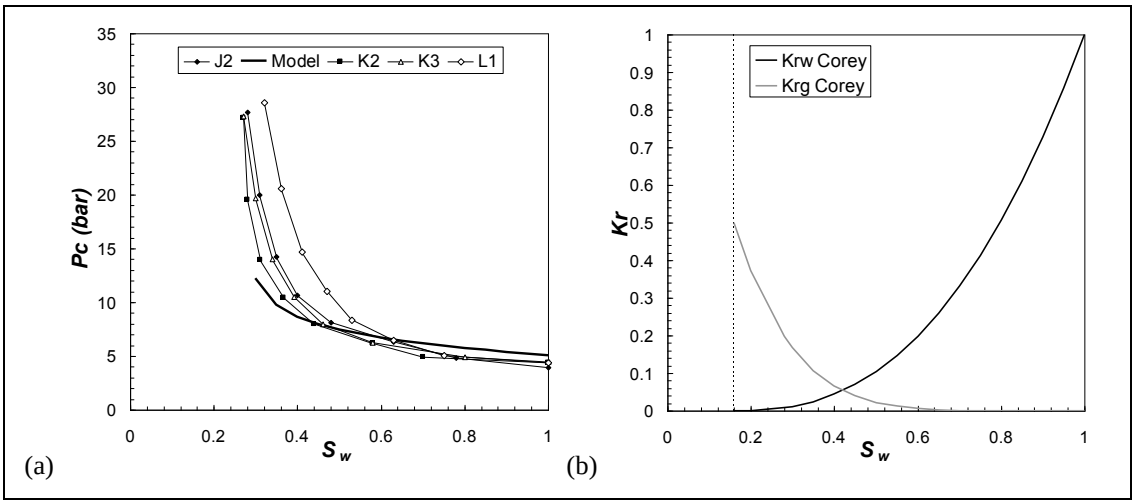

586 (a) (b)

587 *Fig. 5*

588

589

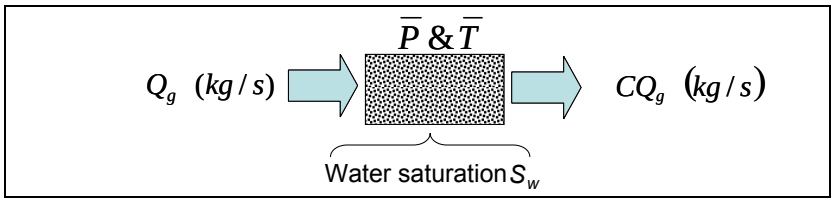

590 Fig. 6

591

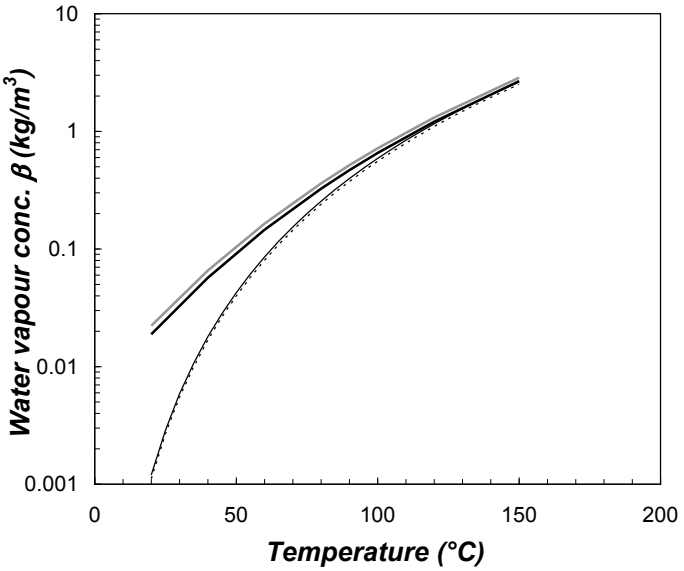

592

593 *Fig. 7*

594

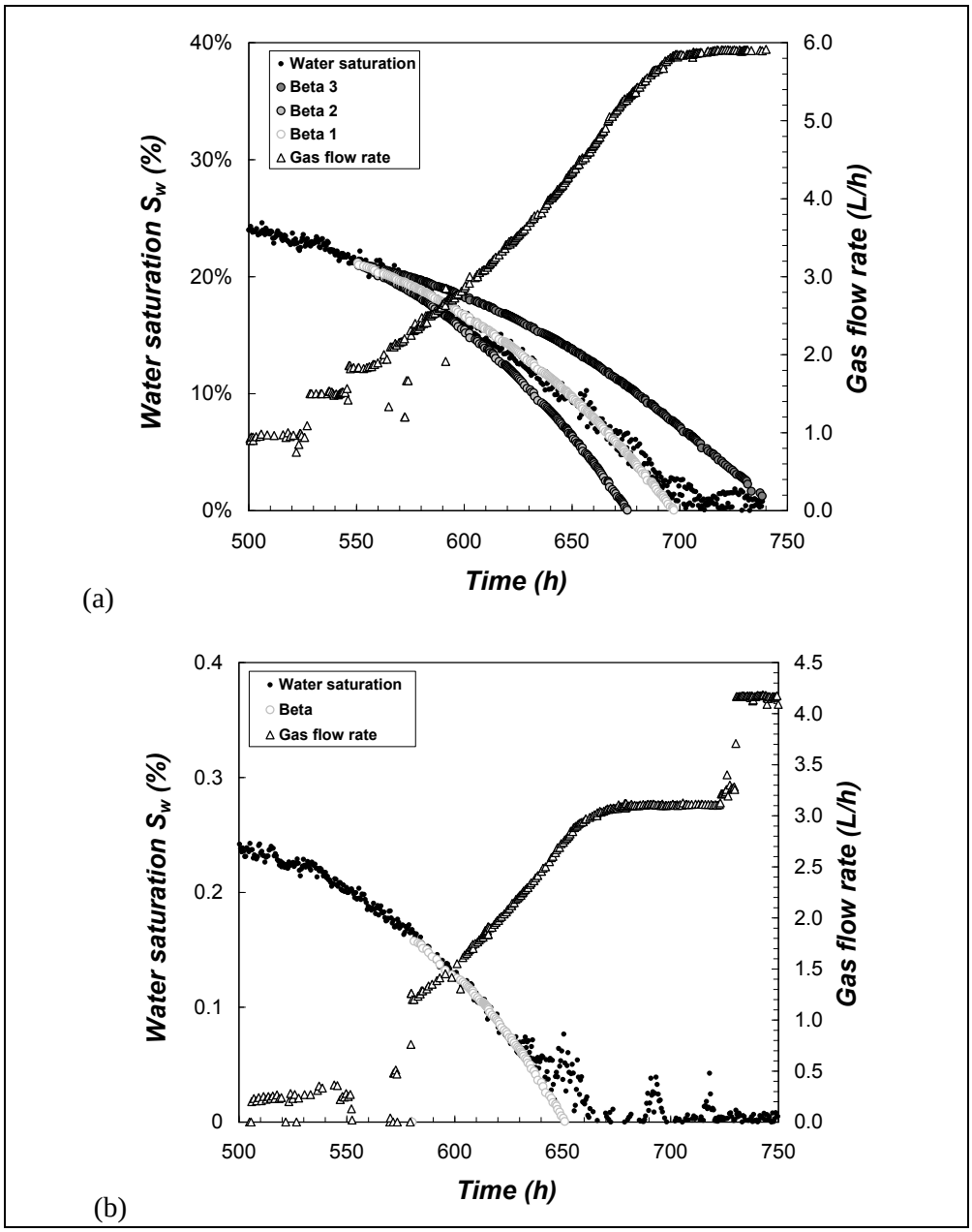
Water saturation
Beta 3
Beta 2
Beta 1
Gas flow rate
Water saturation S_w (%)
Gas flow rate (L/h)
Time (h)
(a)
Water saturation
Beta
Gas flow rate
Water saturation S_w (%)
Gas flow rate (L/h)
Time (h)
(b)

Fig. 8

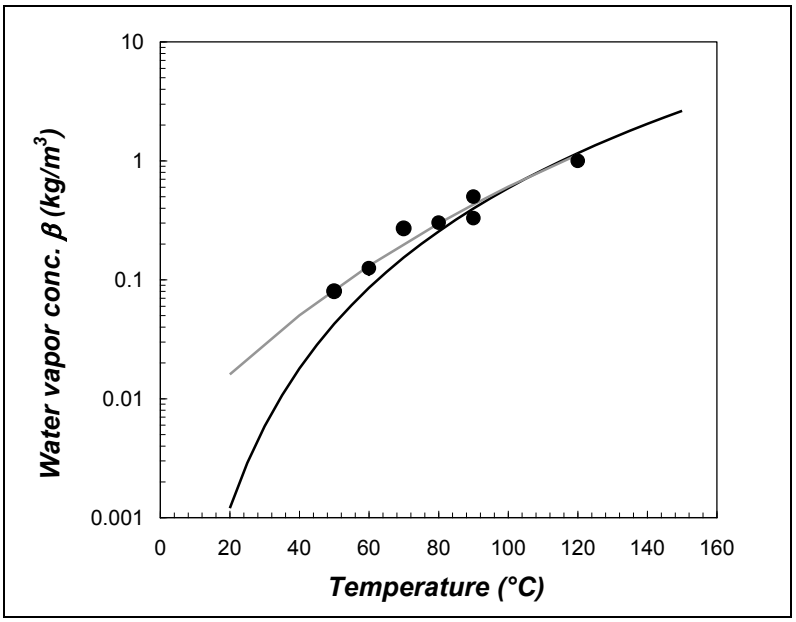

599

600 *Fig. 9*

601

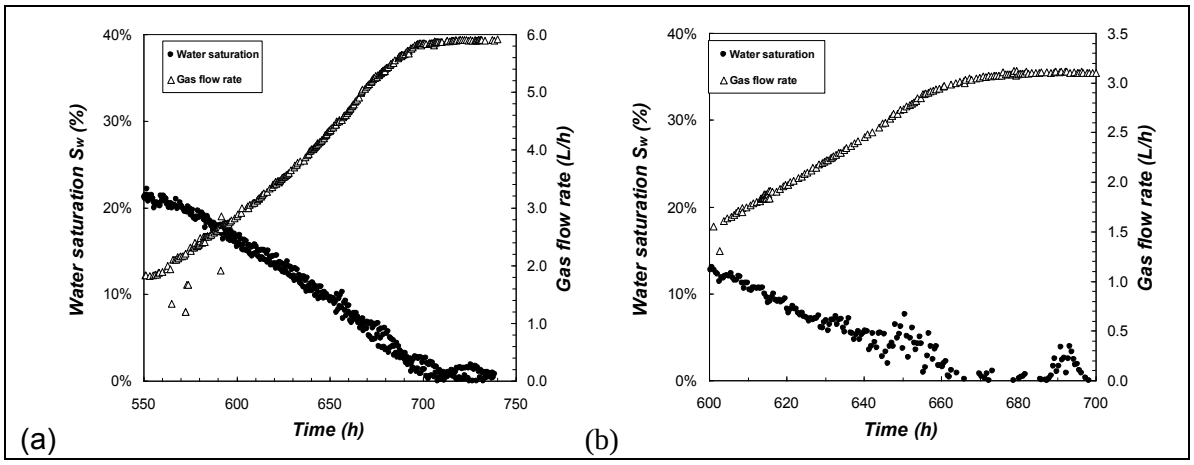
(a)
Water saturation
Gas flow rate
Water saturation S_w (%)
Gas flow rate (L/h)
Time (h)
40%
30%
20%
10%
0%
6.0
5.0
4.0
3.0
2.0
1.0
0.0
550
600
650
700
750
(b)
Water saturation
Gas flow rate
Water saturation S_w (%)
Gas flow rate (L/h)
Time (h)
40%
30%
20%
10%
0%
3.5
3.0
2.5
2.0
1.5
1.0
0.5
0.0
600
620
640
660
680
700

Fig. 10

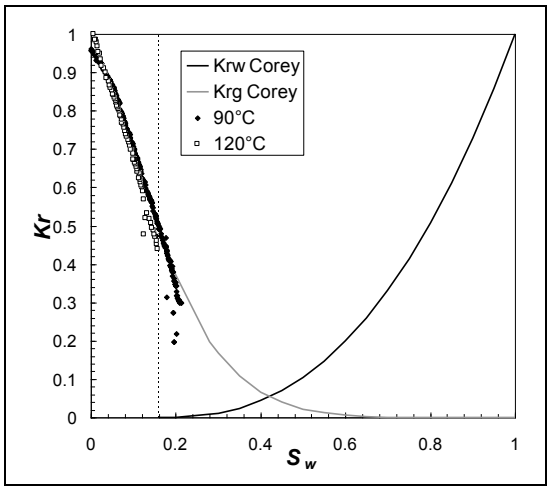

605

606 *Fig. 11*

607

608

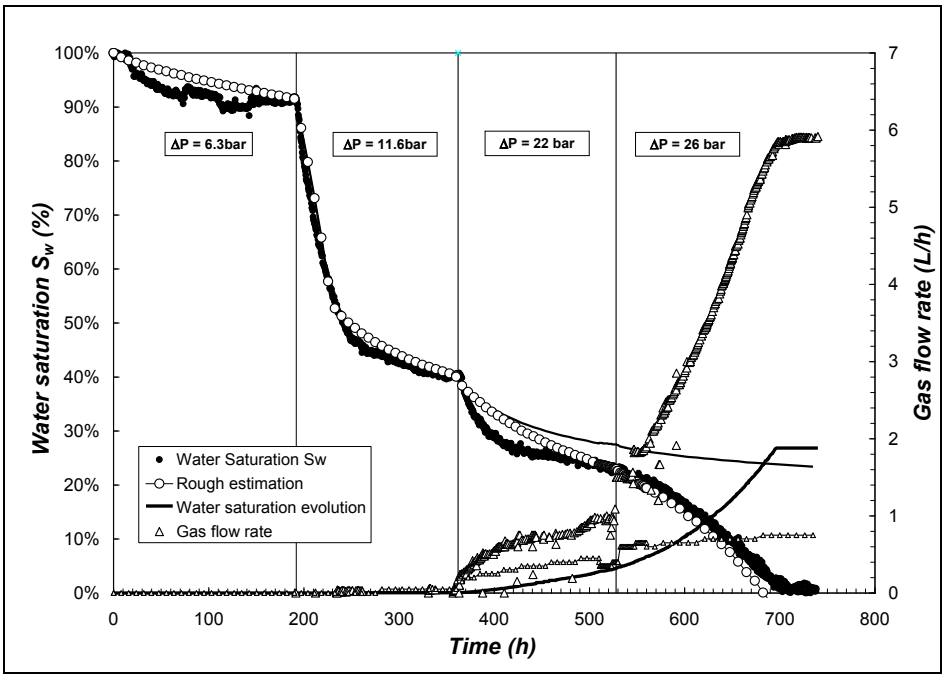

609 *Fig. 12*

610

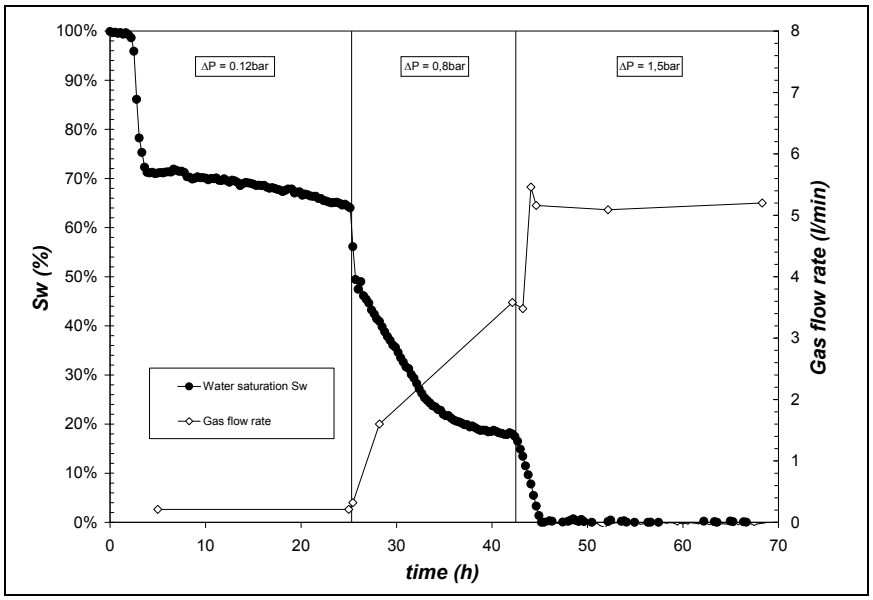

611

612 *Fig. 13*

613

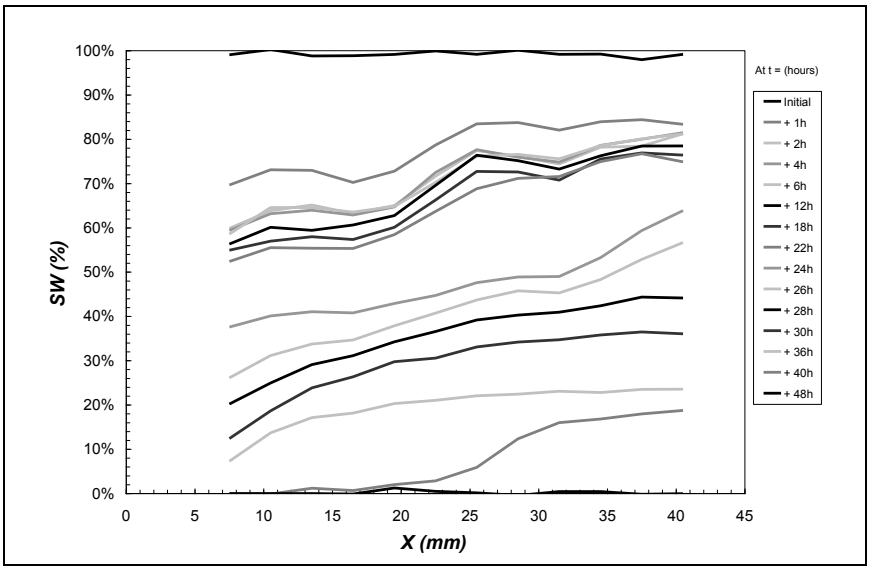

614

615 *Fig. 14*

616

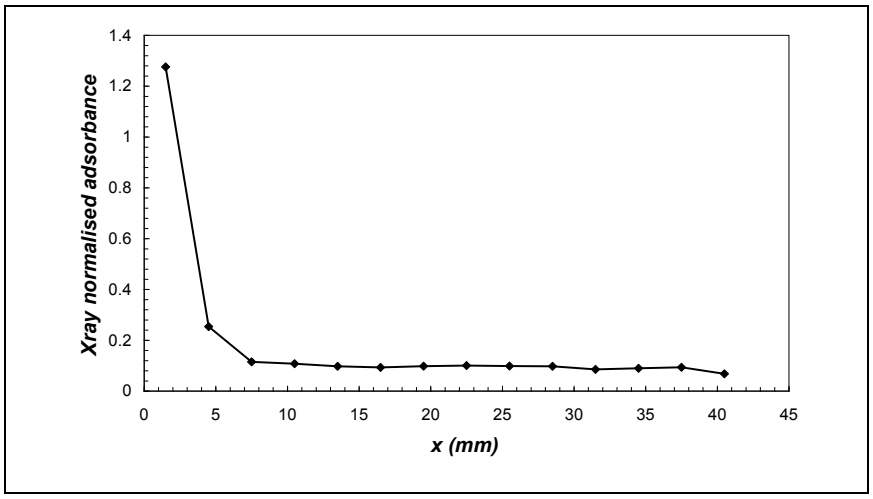

617

618 *Fig. 15*

619

620

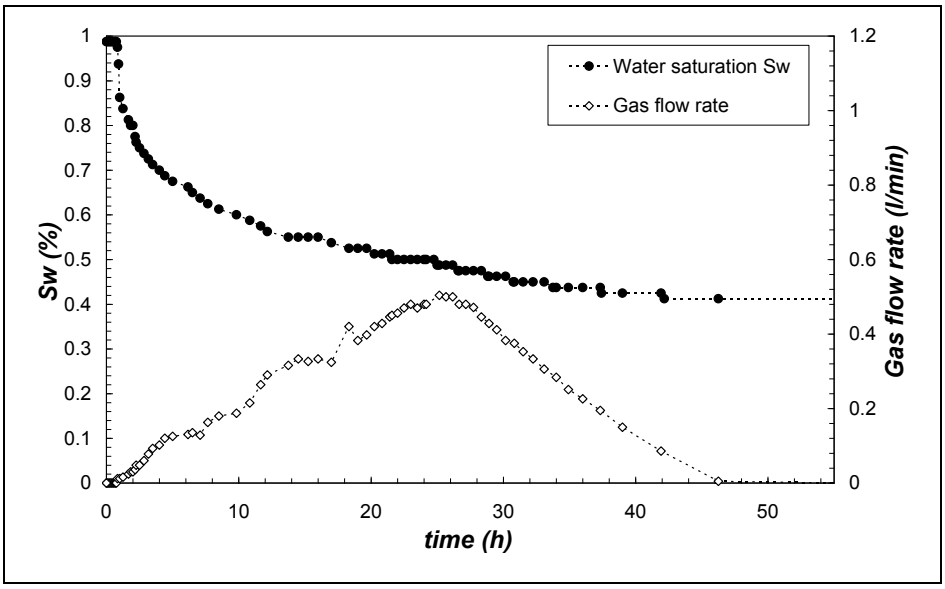

621 *Fig. 16*

622

623 Table 1: Sample characteristics for each experiment.

Rock Sample	*Temperature*	*Brine*	*Initial Porosity*	*Initial permeability*	*Final permeability*
Moliere Sandstone	90°C	Paris basin brine (160g/l TDS)	14%	8 10^{-3} mD	3 10^{-3} mD
Moliere Sandstone	120°C	Paris basin brine (160g/l TDS)	14%	12 10^{-3} mD	6 10^{-3} mD
Vosges Sandstone	80°C	KCl + KI (35g/l TDS)	21.8%	74 mD	22 mD
Vosges Sandstone	60°C	KCl (150g/l TDS)	21.8%	160 mD	0 mD

624

625